INTERNATIONAL JOURNAL OF AUTOMOTIVE AND MECHANICAL ENGINEERING
ISSN: 2229-8649 e-ISSN: 2180-1606
VOL. 21, ISSUE 4, 2024, 11844 – 11856
DOI: https://doi.org/10.15282/ijame.21.4.2024.9.0912

RESEARCH ARTICLE

Metamodel-based Hybrid Parametric Optimization with Static Prototype Validation for a Six-Axle Wheel Load Cell Design

S. Delijaicov[1]*, A. L. S. Gouvêa[1], F. Leonardi[1], A. Farias[1], E. C. Bordinassi[2]

[1]University Center of FEI, São Bernardo do Campo, São Paulo, Brazil
[2]University Center of Maua Institute of Technology, São Caetano do Sul, São Paulo, Brazil

ABSTRACT – The accurate measurement of forces and torques acting on a vehicle's chassis, originating from wheel-pavement interactions, is essential for optimizing suspension systems, axles, and other structural components. A critical challenge in optimizing wheel load cell (WLC) design is to enhance sensitivity without compromising mechanical robustness. To address this question, this study developed a six-axis load cell designed to decouple force and torque measurements, achieving high sensitivity and reliability. The objective was to design an optimized WLC for multi-axis force measurement by maximizing sensitivity through a metamodel-based hybrid optimization framework. The methodology began with a fractional factorial Design of Experiments (DOE) to identify key parameters affecting load cell sensitivity and to define the optimization search space. This was followed by a dual-step parametric optimization process, utilizing the finite element method (FEM) to evaluate load cell performance and an inner-point optimization algorithm for convergence. After completing the DOE and FEM stages, the load cell was physically constructed and calibrated using a universal testing machine MTS 810, where experimental data closely matched simulation results, validating the design's effectiveness. The main findings indicate that the optimized load cell can reliably measure six components, with a sensitivity increase of 14% compared to conventional designs. Numerical results from FEM analyses showed stress levels at 215 MPa, displacements around 0.16 mm, and a first-mode vibration frequency of 1351 Hz, meeting all structural integrity and performance requirements. Calibration confirmed minimal cross-talk effects, supporting the robustness of the final design. The developed load cell met optimal design criteria, showing substantial improvements in sensitivity and accuracy over existing designs, with potential applications in automotive, aerospace, and engineering testing.

ARTICLE HISTORY

Received	:	24th Oct. 2023
Revised	:	27th Sept. 2024
Accepted	:	08th Nov. 2024
Published	:	03rd Dec. 2024

KEYWORDS
Six-axle wheel load cell
Load cell
Metamodel
Parametric optimization
Static validation

1. INTRODUCTION

The need to measure efforts in six axes induced the development of transducers [1] specifically applied to several areas of engineering, such as wind tunnels [2 - 4], structures [5, 6], robotics [7 - 9], biomechanics [10, 11], haptic interaction [12], driver-vehicle interaction [13-14], wheel [15-17] and others. Six-axle wheel force load cells (WLC) are used for dimensioning and experimentally verifying cars' suspension design. It is necessary to design its mechanical components to understand the dynamic influence of the forces and moments acting on the chassis of a vehicle, from the iterations of the wheel to the pavement [18]. Significant works, patents, and commercial six-axis load cells for wheels are already produced, subdivided into two main groups: the transformation of wheels into load cells [19] and the development of dynamometric cubes [16, 20]. Both categories are segmented according to the type of sensitive element used, such as resistive, capacitive, piezoresistive, and piezoelectric sensors. The resistive load cells are current in these applications due to their low cost, ease of instrumentation, and measurement in static or dynamic loads.

A critical point in designing multiaxial force load cells is to ensure the absence of cross-talking, that is, the interference of one measurement channel on the others. Researchers have tried reducing the effects of cross-talking in dynamometric cubes using two principal methodologies: the first, based on the structural optimization that eliminates the coupling of the forces and moments acting on the wheel [16], and the second, based on the mitigation of the signal interference, to minimize the experimental error by the use of several algorithms [21 - 23]. The errors generated by the simplifications and dimensional approximations imply a decrease in the precision of the measurements made by the load cells. These errors can be divided into two main areas of study: the first is related to design in the choice of the quantity and positioning of the strain gages, and the second is linked to the dimensional uncertainties of the force load cell [16].

When discussing the technology for measuring forces and moments in road vehicles, its significance for automotive engineering becomes evident. [24] investigated the measurement of forces and moments at various locations on cars, emphasizing its impact on active safety and stability-enhancing systems, such as Advanced Driver Assistance Systems (ADAS) and fully automated driving. A nonlinear decoupling method utilizing a high-order polynomial model for wheel load cells was introduced by [25]. This method reduces the coupling error between axles and is based on an eight-beam structure that employs multiple linear regression to enhance accuracy, achieving a maximum error of 44%. Simultaneously,

***CORRESPONDING AUTHOR | S. Delijaicov** | ✉ sergiode@fei.edu.br
© 2024 The Author(s). Published by Universiti Malaysia Pahang Al-Sultan Abdullah Publishing. This is an open access article under the CC BY-NC 4.0 International license

[26] presented a wheel load cell calibration approach aimed at improving accuracy through an interpretable nonlinear decoupling model. This model, developed within a primary error polynomial framework and utilizing a hyperbolic activation function, demonstrated comparable accuracy to more complex models like neural networks but required fewer parameters, suggesting a more efficient calibration method.

A numerical analysis approach for optimizing Wheel Force Transducer (WFT) component structures using selective laser melting manufacturing was developed by [27]. This approach allows for the creation of lightweight, complex components with superior performance for dynamic and stability analyses. The reported results indicate a weight reduction of nearly 40% while maintaining the original stiffness, which is crucial for operational safety. However, [28] notes that existing decoupling models fail to fully describe the coupling process of the Reactive Multi-Force Sensor (RMFS) when subjected to centralized loads, a common scenario for off-road Wheeled Mobile Robots navigating challenging terrains. The authors propose a corrected decoupling model that incorporates elastic stresses as an intermediate variable, replacing the original rotation matrix with a corrected matrix whose elements are odd harmonic functions. This approach aims to reduce coupling errors resulting from centralized loads. Calibration experiments demonstrated that the corrected model decreased the variance of the calibration error rate from 1.95% to 0.054% compared to a machine learning-based decoupling model.

To achieve high stiffness, sensitivity, and minimal coupling, [29] proposed a Force Wheel Transducer featuring a crossbeam elastomer design made from titanium alloy. The paper introduces a Back Propagation-Particle Swarm Optimization (BP-PSO) decoupling algorithm that enhances the optimization process of a Back Propagation neural network. This algorithm aims to improve the decoupling of inter-dimensional data, addressing a challenge in accurately measuring force and torque across multiple axes. The sensor design achieves a sensitivity of 4 mV/V and reports improvements in accuracy with crosstalk reduction, with crosstalk values notably below 5% in the vertical force direction, marking an advancement in minimizing interference between measurement axes. In data acquisition and design methodology, [30] implemented a six-axis force/moment (F/M) sensor integrated with a high-efficiency data acquisition (DAQ) system.

This work proposes a hybrid framework based on fractional factorial experiment and nonlinear parametric optimization, subject to mechanical and geometric constraints, to get the maximum sensitivity in acquiring the forces acting on the load cell. This proposal is considered innovative compared to previous research that only integrated DAQs in capacitive and optical sensors. The structural design of the sensor was optimized using the parametric optimization process method and validated through FEM.

2. HYBRID FRAMEWORK

2.1 Forces and Moments Components

The proposed methodology elaborates on a numerical model capable of ascertaining the performance and characteristics of wheel force load cells. These devices can measure three forces and moments caused by the tire and track iterations. Figure 1(a) represents the six loads generated in the contact region of the tire, three referring to the forces and three related to the moments and Figure 1(b) presents the six resulting loads in the center of the wheel.

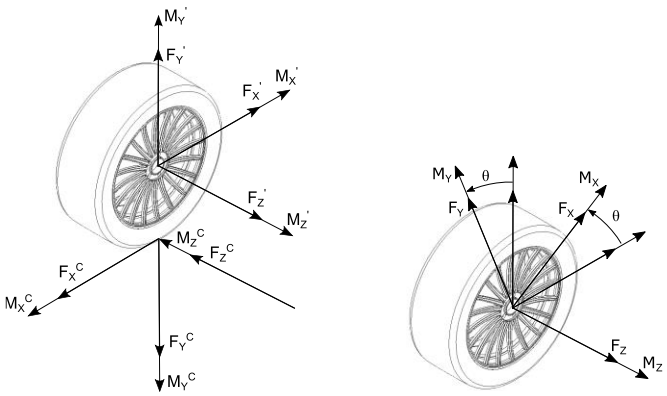

(a) (b)

Figure 1. Main forces acting on a generic wheel, a) forces acting on a generic wheel; b) reference of a wheel force load cell

The components of forces and moments (FX; FY; FZ; MX; MY; MZ) expressed by the vector {F'}, which is associated with the orthogonal base adopted (Eq. 1), are the quantitative variables obtained by the load cell.

$$\{F'\}=\begin{Bmatrix} F_X' \\ F_Y' \\ F_Z' \\ M_X' \\ M_Y' \\ M_Z' \end{Bmatrix}=\begin{bmatrix} \cos\theta & -sen\theta & 0 & 0 & 0 & 0 \\ sen\theta & \cos\theta & 0 & 0 & 0 & 0 \\ 0 & 0 & 1 & 0 & 0 & 0 \\ 0 & 0 & 0 & \cos\theta & -sen\theta & 0 \\ 0 & 0 & 0 & sen\theta & \cos\theta & 0 \\ 0 & 0 & 0 & 0 & 0 & 1 \end{bmatrix}\begin{Bmatrix} F_X \\ F_Y \\ F_Z \\ M_X \\ M_Y \\ M_Z \end{Bmatrix} \tag{1}$$

where θ is the angle between the vehicle's fixed frame and the wheel's orthogonal base system. The variation concerning the X and Y axes of the car is the same, thus guaranteeing the condition of perpendiculars in the Cartesian system.

Strain gages are generally used as embedded devices in the construction of load cells because they are small, light, accurate, and relatively inexpensive. With a structure loaded at a given point by a vector of forces $\{F\}$, the load cell will produce output signals according to Eq. (2):

$$\{S\} = \{S_1; S_2; S_3; \dots S_{f-1}; S_f\}^T \tag{2}$$

The conformity of strains portrays the relationship between the field of strains measured in the load cell and the imposed loading vector using the relation (Eq. 3): [31],

$$\{S\} = [C_n]_{n\times 6}\{F\} \tag{3}$$

where $[C_n]$ represents the normalized conformity matrix of deformations. The solution of Eq. (3) for $\{F\}$ is:

$$\{F\} = [C_n]_{6\times 6}{}^{-1}\{S\} = [B_n]_{6\times 6}\{S\} \tag{4}$$

where $[B_n]$ symbolizes the calibration matrix of the sensor, a direct relationship between measured strength and signal strength. The normalized conformity matrix $[C_n]$ can be determined by the formulation expressed by Eq. (5) [31],

$$c_n(i,j) = \frac{c(i,j)}{f(j)} \tag{5}$$

That represents the maximum design force in the considered direction.

According to [32], a slight relationship between the maximum and minimum eigenvalues of the calibration matrix of the device causes the strain compliance matrix to have a more uniform and more accurate behavior. The isotropy index of C_0, given by Eq. (6), can calculate this condition.

$$C_0 = \frac{\varphi_1}{\varphi_6} \tag{6}$$

where φ_1 and φ_6 refer to the principal eigenvalues of the load cell compliance matrix, respectively. This characteristic is also valid for the calibration matrix [Bn]. The isotropic index depends on the device's structural configuration, the strain gages' positions on the load cell, and the maximum design forces for the load cell. This parameter is expected to be closer to 1, thus ensuring that the device has a good homogeneity in its measurements and mitigating errors while forming the conformity matrix [C] [31].

If the variable $[C_n]$ is not purely diagonal, the effects of cross-talking between the loading forces directly influence the sensor's calibration matrix calculation. These coupling variations $[CSC]$ can be accounted for according to Eq. (7) expressed in [31]:

$$CSC(i,j) = \frac{c_n(i,j)}{\sum_{j=1}^{6}|c_n(i,j)|} \tag{7}$$

The strains obtained in the output signal of a load cell are not directly acquired and, therefore, must be measured using electric circuits [31]. One of the most used circuits is the Wheatstone bridge, which uses complete configuration. It is assumed that all gages present in the circuit have the same magnitude of Strain (ε), defined as Eq. (8):

$$\varepsilon = \frac{V_s}{K_s V_e} \tag{8}$$

The bridge sensitivity $[S_e]$ of a bridge is given by Eq. (9):

$$S_e = \frac{V_s}{V_e} \tag{9}$$

where V_s and V_e are the output and input voltages, respectively, substituting Eq. (8) into (9) gives:

$$S_e = K_s\varepsilon \tag{10}$$

A sensitivity greater than 1.0 mV / V is considered reasonable for general load cell applications using metallic Strain gages [31]. In multiaxial force load cells, the sensitivity parameter is used to quantify the total deformation measured in the electric circuit. Thus, according to [33], sensitivity can be obtained in the load cells by:

$$S_e = \|C_i\| \tag{11}$$

where $\|C_i\|$ represents the Euclidean standard of the i-th line of the strain compliance matrix.

2.2 Force Load Cell

The geometry adopted in the wheel is based on a design performed at the University of Pretoria [23], and the geometric characteristics of the final assembly of the device is presented in Figure 2, a load cell coupled in a SAE (Society of Automotive Engineers) Baja car.

Figure 2. Exploded view of the final assembly and the SAE Baja car

According to Figure 3, the proposed WLC is characterized by (i) four deformable structures, the beams; (ii) four regions of flexibility, the plates; (iii) the central region, where the external loads are applied to the assembly and (iv) the area of attachment, sector of coupling of the component to the vehicle's wheel. Therefore, nine independent geometric parameters were defined (Figure 3). These constitute the structural basis of the load cell base geometry.

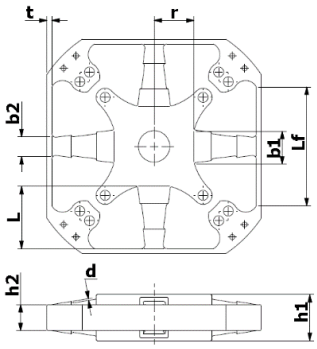

b_1	base of the sensitive element in the central region
b_2	base of the sensitive element at the extremity
h_1	height of the sensitive element in the central region
h_2	height of the sensitive element at the extremity
L	length of the sensitive element
L_f	length of the plate structure
t	plate structure thickness
d	sensitive element groove
r	distance from the beginning of the sensitive element to the central region

Figure 3. Detail of the parameters of the load cell structure

The material adopted for this design was AA7075-T6 aluminum alloy, and Table 1 shows the mechanical properties.

Table 1. Mechanical properties - AA7075 - T6

Mechanical characteristics – AA7075-T6	
Modulus of elasticity – E	71.7 GPa
Poisson coefficient - ν	0.33
Density - ρ	2810.0 kg / m³
Yield stress - σ_{esc}	503.0 MPa
Mechanical resistance stress - σ_{res}	572.0 MPa
Fatigue stress - σ_{fad} *	185.0 MPa

*Mechanical parameter for $5x10^9$ completely reverses fatigue cycles

2.3 Model

The load cell stress numerical solution model was element size 1.5 mm, method tetrahedrons, nodes 460023, and elements 299577. The load vector was based on the values usually used to design the entire SAE Baja car set, as follows: Force X = 5500N, Force Y = 4268N, Force Z = 2132 N, Torque X = 50 Nm, Torque Y = 50 Nm and Torque Z = 1485 Nm.

A sketch is shown in Figure 4(a) for identifying the 24 strain gage's location points employed in the acquisition system, and Figure 4(b) for the respective six strain measurement bridges.

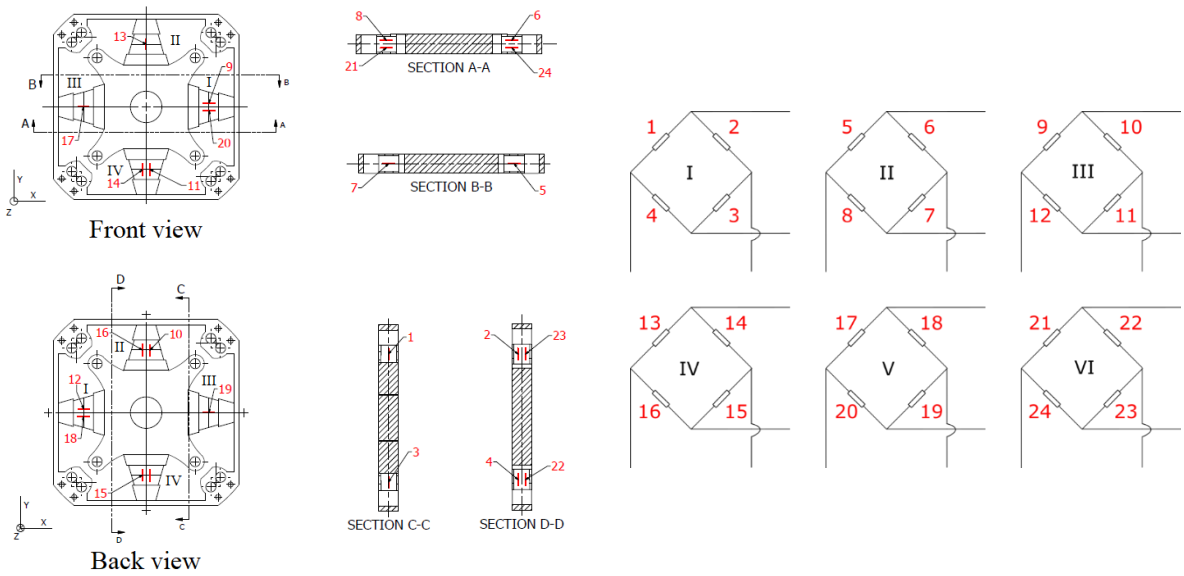

(a) (b)

Figure 4. (a) Positioning of the Strain gages in the structure of the force load cell, and (b) bridges I to VI measure the forces *F*x, *F*y, *F*z, and moments *M*x, *M*y, and *M*z, respectively

2.4 Parametric Optimization

The objective of the methodology is to maximize the total load cell sensibility of (Eq. 11) and can be expressed by the objective function Eq. (12):

$$f_1(x) = (\|C_1\| + \|C_2\| + \|C_3\| + \|C_4\| + \|C_5\| + \|C_6\|), \tag{12}$$

The indices of the deformation conformance matrix represent the sensitivity of each of the six channels of the load cell, shown in Figure 4 and Eq. (13):

$$\begin{aligned}
c_{1,j} &= \frac{1}{4}(\varepsilon_1 - \varepsilon_2 + \varepsilon_3 - \varepsilon_4) && j = 1\ to\ 6\\
c_{2,j} &= \frac{1}{4}(\varepsilon_5 - \varepsilon_6 + \varepsilon_7 - \varepsilon_8) && j = 1\ to\ 6\\
c_{3,j} &= \frac{1}{4}(\varepsilon_9 - \varepsilon_{10} + \varepsilon_{11} - \varepsilon_{12}) && j = 1\ to\ 6\\
c_{4,j} &= \frac{1}{4}(\varepsilon_{13} - \varepsilon_{14} + \varepsilon_{15} - \varepsilon_{16}) && j = 1\ to\ 6\\
c_{5,j} &= \frac{1}{4}(\varepsilon_{17} - \varepsilon_{18} + \varepsilon_{19} - \varepsilon_{20}) && j = 1\ to\ 6\\
c_{6,j} &= \frac{1}{4}(\varepsilon_{21} - \varepsilon_{22} + \varepsilon_{23} - \varepsilon_{24}) && j = 1\ to\ 6
\end{aligned} \tag{13}$$

2.5 Constraints

The inequalities constraints (Figure 5) are imposed as functions limiting the design of the load cell and are fragmented into two main groups, the geometric constraints, exclusively dependent on the wheel dimensions, and the mechanical limitations linked to the responses obtained in the structure of the load cell. The dimensional inequality constraints confirm that the load cell, obtained during the parametric optimization procedure, will comprise the wheel's internal region.

$$\begin{aligned}
g_1(x) &= h_1 - 60 & 10 \le b_1 \le 40\\
g_2(x) &= h_2 - 60 & 10 \le b_2 \le 40\\
g_3(x) &= \left(L - \frac{t}{2}\right) + r - \frac{176}{2} & 10 \le h_1 \le 40\\
g_4(x) &= \frac{L_f}{2} + 15 - \frac{176\sqrt{2}}{2} & 10 \le h_2 \le 40\\
g_5(x) &= \frac{d}{\min(h_1, h_2, b_1, b_2)} - 0{,}10 & 41 \le L \le 52\\
g_6(x) &= \sigma_{VM\max} - \frac{\sigma_{fad}}{F_c} & 41 \le L_f \le 94\\
& & 0.5 \le t \le 8\\
& & 1.5 \le d \le 8\\
& & 30 \le r \le 32
\end{aligned}$$

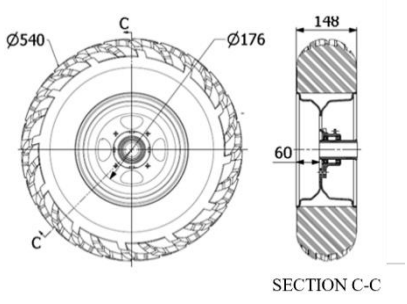

Figure 5. Mechanic and geometric constraints imposed by the vehicle wheel

2.6 Hybrid Optimization

Since the optimization problem is nonlinear and non-convex, its numerical solution depends on the initial estimate. One must choose a favorable region to start the gradient-oriented search. The proposed methodology employs fractional planning of design of experiments (DOE) simulation to obtain an initial estimate for an optimization problem that uses the same design variables as the DOE. The formulated optimization problem involves the determination of the total load cell sensibility using the finite element method (FEM).

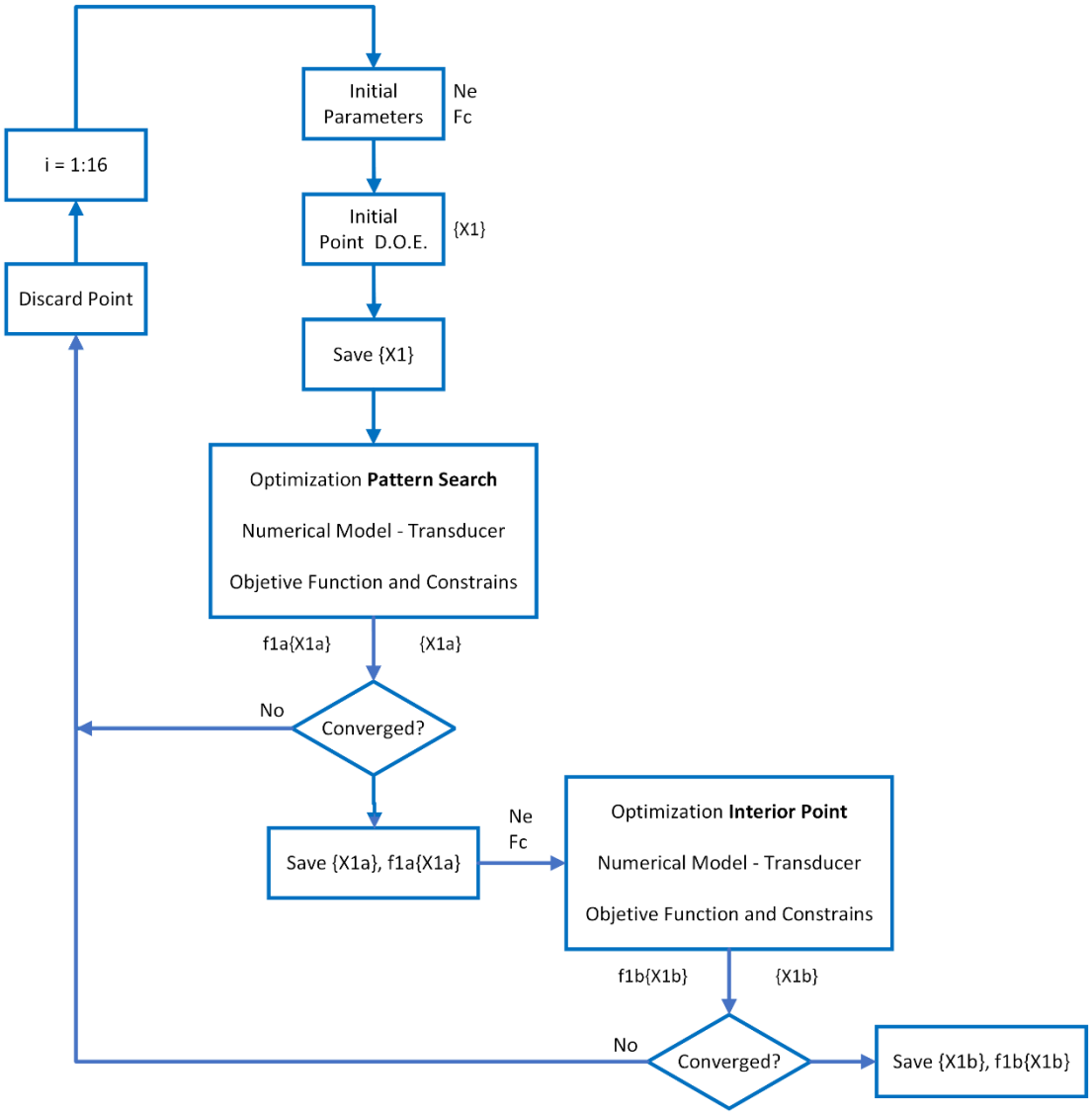

Figure 6. Algorithm of the hybrid optimization method

Since there is no guarantee of convergence of the optimization problem, the proposed method incorporates a scheme of redefining the ranges of the DOE variables whenever convergence fails. When convergence occurs, we offer to solve a new optimization problem based on the previous convergence. The second optimization is conducted using a method different from the first one, expecting that the local minimum obtained differs from the first. Again, convergence failure may occur, forcing a new choice of number range for the DOE, and the process repeats from the beginning. When both optimization schemes converge, the more extreme value is chosen as the solution. The flowchart in Figure 6 illustrates the proposed methodology.

The Statistica® software obtained the fractional factorial experiment methodology points. The contours of the system are defined by the limits of the parametric optimization routine and can be visualized in Table 2. The sub-optimum sensitivities obtained with the design of experiments are used as starting points of the parametric optimization routine using the Inner Point Optimization Algorithm. The endpoint of the iteration is defined as the acceptable optimal condition of the system [34].

Table 2. The fractional factorial parameters

Points	b1	b2	h1	h2	L	Lf	t	d	r
1	10	40	40	40	41	94	0.5	1.5	30
2	10	10	10	40	41	94	8.0	8.0	30
3	10	40	10	10	52	94	0.5	8.0	30
4	10	40	10	40	52	41	8.0	1.5	32
5	40	10	10	40	52	94	0.5	1.5	32
6	40	40	40	40	52	94	8.0	8.0	32
7	10	10	40	10	52	94	8.0	1.5	30
8	40	10	40	10	41	94	0.5	8.0	32
9	40	10	10	10	52	41	8.0	8.0	30
10	40	40	10	40	41	41	0.5	8.0	30
11	10	40	40	10	41	41	8.0	8.0	32
12	40	40	40	10	52	41	0.5	1.5	30
13	40	10	40	40	41	41	8.0	1.5	30
14	10	10	10	10	41	41	0.5	1.5	32
15	10	10	40	40	52	41	0.5	8.0	32
16	40	40	10	10	41	94	8.0	1.5	32

3. RESULTS AND DISCUSSIONS

The sub-optimum sensitivities obtained by the experimental design method (Figure 6) are shown in Table 3.

Table 3. Objective functions at the points defined by the experimental design

	Total sensibility [mV/V]		Total sensibility [mV/V]
Experiment 1	4.014	Experiment 9	0.335
Experiment 2	0.279	Experiment 10	1.175
Experiment 3	2.539	Experiment 11	0.726
Experiment 4	0.335	Experiment 12	3.598
Experiment 5	3.877	Experiment 13	5.329
Experiment 6	1.488	Experiment 14	4.071
Experiment 7	0.313	Experiment 15	1.044
Experiment 8	4.403	Experiment 16	4.049

Considering experiment #13, which presented the best sub-optimal solution of the experimental design, the results of the available load cell and the project variables are presented in Figure 7 and Table 4. Figure 7 presents the results for experiment #13, highlighting three aspects: Figure 7 (a) the von Mises stress criterion, which illustrates the distribution of stress within the material. Figure 7 (b) shows the displacements, indicating how the material deforms under applied forces. Figure 7 (c) is the first vibration mode, indicating the primary frequency at which the structure vibrates.

The mechanical analysis of the load cell model produced significant values regarding its structural integrity and performance characteristics when subjected to simulated conditions. In Figure 7(a), the von Mises stress distribution revealed stress levels approaching approximately 215 MPa at the base of the sensitive element within the load cell. In addition to the stress analysis, Figure 7(b) shows that the displacement analysis indicated an approximate movement of 0.16 mm in the sensitivity regions of the load cell. This displacement measurement is especially relevant as it highlights the areas where external forces most affect the component. Therefore, these locations are the most appropriate for the load cell instrumentation. In Figure 7(c), the analysis of the component's vibrations at 1351 Hz provided essential insights into its dynamic behavior, particularly in the first vibration mode. This frequency represents a key resonance point, where the structure is more prone to oscillations. The resulting value is close to that obtained by Nouwens [23].

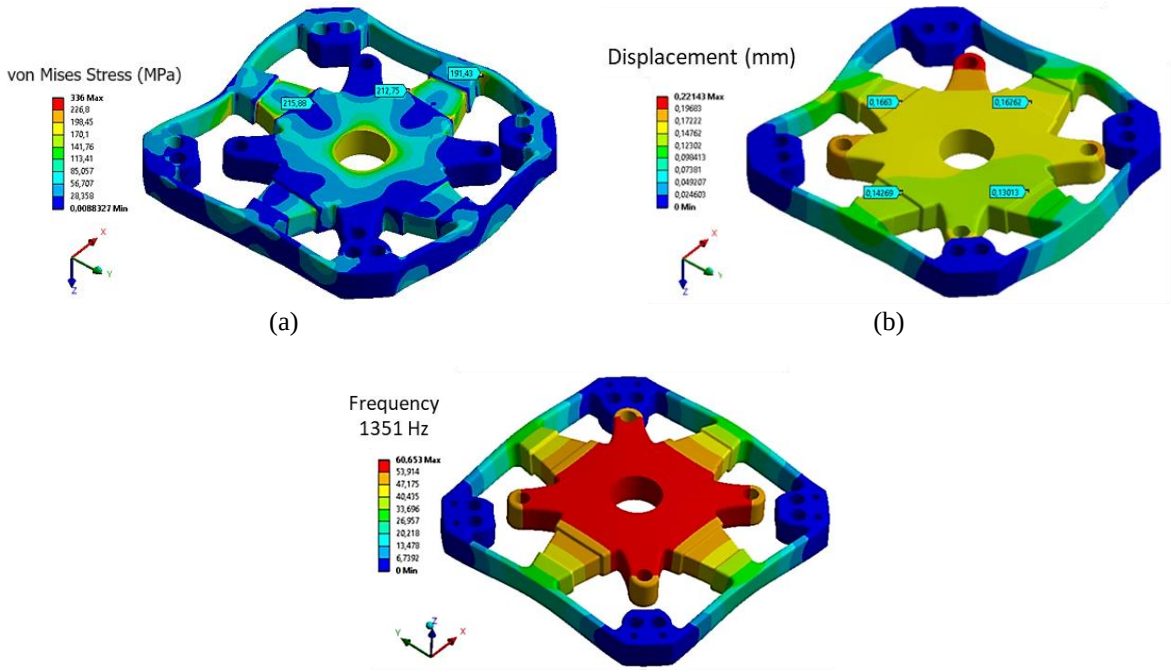

(a) (b)

(c)

Figure 7. Results for experiment 13, (a) von Mises Stress criterion, (b) displacements and (c) first vibration mode

Table 4. Summary of parametric optimization results for experiment 13

Variable	Value	Variable	Value
b_1 [mm]	37.74	Von Mises Stress [MPa]	131.0
b_2 [mm]	15.42	Displacement [mm]	0.163
h_2 [mm]	15.29	Natural Frequency [Hz]	1351
L [mm]	41.75	Sensitivity - Channel 2 [mV / V]	1,180
L_f [mm]	94.00	Sensitivity - Channel 2 [mV / V]	0.916
t [mm]	4.26	Sensitivity - Channel 3 [mV / V]	0.426
d [mm]	1.47	Sensitivity - Channel 4 [mV / V]	0.258
r [mm]	29.96	Sensitivity - Channel 5 [mV / V]	0.258
b_2 [mm]	15.42	Sensitivity - Channel 6 [mV / V]	2.288
L [mm]	41.75	Sensitivity – Total [mV / V]	5.326

The most influential parameter in determining the sensitivity is the groove of the sensitive element **d** since it is directly related to the region of installation of the gages present in the system of acquisition of the load cell. Consequently, any alteration in this region interferes intensively with the result obtained. However, it was found that the system is limited by the restriction of the maximum working stress, which makes it impossible to reduce the dimension of the beam, which would result in a higher sensitivity of the measured signal.

Another dominant parameter is the thickness in the region of the plates. It directly influences the rigidity of the device, thus mitigating the strains obtained in the sensitive elements. The measured stress, close to the region between the boards and the beams, restricts parameter **d**. Variable b1 is directly related to the moments of inertia in the structure of the sensitive element. Therefore, any variation in this parameter interferes punctually with the system's sensitivity. However, like the other parameters, it is delimited by the stresses and the geometric constraint imposed on the system. The length of the component's sensitive element, in the same way, that the plate thickness parameter, affects the system rigidity, and its increment makes it more flexible. At the same time, its decrease imposes a greater rigidity on the assembly. The $\mathbf{b_2}$, **r,** and $\mathbf{h_2}$ parameters are less sensitive in determining the deformations. Then, the normalized compliance matrix is:

$$[C_n] = \begin{bmatrix} 0.1020 & 0 & 0 & 0.0003 & 0 & 0 \\ 0 & 0.1020 & 0 & 0 & 0.0003 & 0 \\ -0.0001 & 0.0001 & 0.0947 & 0 & 0 & 0 \\ -0.0060 & 0 & 0 & 0.0025 & 0 & 0 \\ 0 & 0.0060 & 0 & 0 & 0.0025 & 0 \\ 0.0001 & -0.0001 & 0.0204 & 0 & 0 & 0.0073 \end{bmatrix} \times 10^{-6} \quad (14)$$

The inverse of the strain compliance matrix gives the calibration matrix of the force load cell is:

$$[B_n] = \begin{bmatrix} 0.0097 & 0 & 0 & -0.0011 & 0 & 0 \\ 0 & 0.0099 & 0 & 0 & -0.0011 & 0 \\ 0 & 0 & 0.00106 & 0 & 0 & 0 \\ 0.0236 & 0 & 0 & 0.3994 & 0 & 0 \\ 0 & -0.0239 & 0 & 0 & 0.4045 & 0 \\ -0.0017 & 0.0017 & 0.2943 & 0 & 0 & 1.3624 \end{bmatrix} \times 10^9 \tag{15}$$

The isotropic index can be verified according to the result presented by:

$$C_0 = 8{,}84 \tag{16}$$

Subsequently, there is cross-talk in the load cell acquisition system, according to:

$$[CSC] = \begin{bmatrix} 0.9983 & 0 & 0 & 0.1074 & 0 & 0 \\ 0 & 0.9983 & 0 & 0 & 0.1074 & 0 \\ 0.0010 & 0.0010 & 0.9774 & 0 & 0 & 0 \\ 0.0580 & 0 & 0 & 0.9942 & 0 & 0 \\ 0 & 0.0589 & 0 & 0 & 0.9942 & 0 \\ 0.0010 & 0.0010 & 0.2111 & 0 & 0 & 0.9999 \end{bmatrix} \tag{17}$$

The sensitivity vector of the acquisition system is:

$$\{S_e\} = \begin{Bmatrix} 1.18 \\ 0.92 \\ 0.43 \\ 0.26 \\ 0.26 \\ 2.29 \end{Bmatrix} \text{mV/V} \tag{18}$$

Therefore, the vector of forces measured by the load cell is:

$$\{F\} = \begin{Bmatrix} 5500 \\ 4268 \\ 2132 \\ 50000 \\ 50000 \\ 1485000 \end{Bmatrix} \text{N} \tag{19}$$

The first three parameters in Eq. 19 are related to the design forces and are in N, while the others represent the moments imposed on the model in Nm. The techniques used to validate the load cell numerical model were:

a) Three-dimensional model resolution of the load cell by the finite element method using Ansys ® software;
b) Load cell calibration after construction and instrumentation (Figures 8, 9, and 10) using HBK's QuantumX Data Acquisition System. The force transducer calibration values, in N and Nm, presented in Table 5, were calculated for the standard sensitivity of 2 mV/V, corresponding to a strain of 4000 x 10^{-6} in the Wheatstone bridge for each measurement channel. One can notice a good agreement between the values of the efforts and the values of the models. The inconsistencies are due to the errors obtained from the reverse operation performed under the strain conformance matrix.

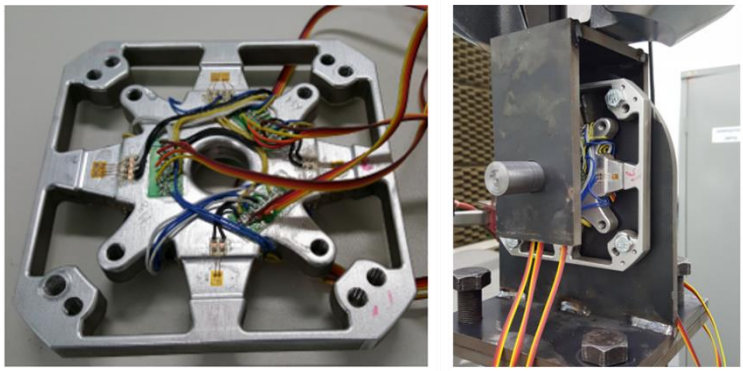

(a) (b)

Figure 8. (a) Load cell instrumentation and (b) calibration test

Figure 8(a) presents the load cell meticulously prepared and instrumented adequately with strain gauges positioned at the specific points of interest. These points were identified based on the simulation of the displacements observed in Figure 7(b), which corresponded to the base of the sensitive element within the load cell. In addition, Figure 8(b) illustrates the

load cell once it had been mounted onto the adaptation device designed for installation on the MTS 810 universal testing machine. The MTS 810 machine was utilized to apply the various loads necessary during the calibration process of the load cell. The adaptation device's design was executed carefully to ensure a robust and secure attachment to the grips of the MTS 810 universal testing machine. Furthermore, it also guaranteed the precise centralization of the load cell on the MTS 810, thus enhancing the accuracy and reliability of the testing and calibration procedures.

Figure 9 displays the calibration curves for channels 1, 2, and 3, each represented by distinct colors and corresponding loading points. Channel 1, in red, utilizes four loading points for calibration purposes, while channel 2, in blue, incorporates five loading points for its calibration curve. Channel 3, shown in black, also employs five loading points for calibration. All calibration loads were generated using the MTS 810 universal testing machine. The calibration methodology involved linear regression to model the relationship between the dependent Strain measured in micrometers (μm) on the load Force (N). The resulting regression equations for each channel have been included alongside the legends for each respective channel, providing a comprehensive overview of the relationships established through the calibration process. Channels 1 and 2 exhibited similar behavior with an approximate strain limit of 3500 (μm) and channel 3's strain limit of approximately 1500 (μm).

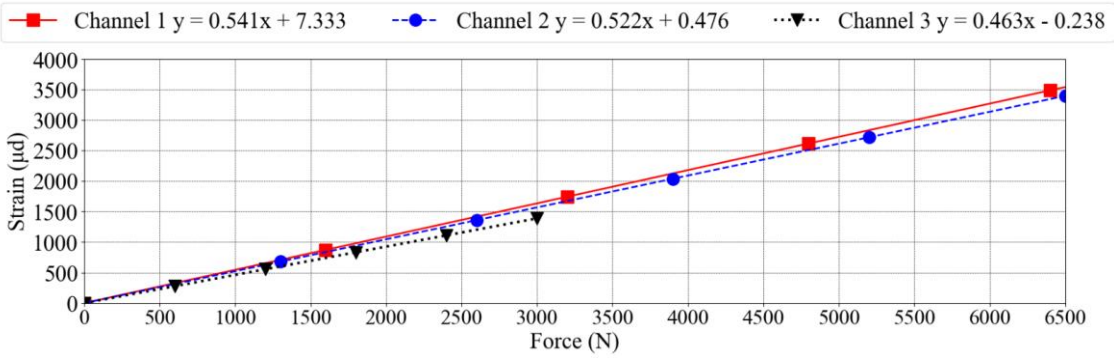

Figure 9. Calibration curves for channels 1, 2 and 3

Figure 10 presents the calibration curves for channels 4, 5, and 6, showing their respective load points and strain limits. Channel 4 is represented in red and was calibrated using five load points, while channel 5, displayed in blue, also underwent calibration with five load points. Channel 6, shown in black, was calibrated with only two load points. All calibrations were performed using the MTS 810 universal testing machine, employing a linear regression method to fit the data. The regression equations for each channel are provided in the legend next to their corresponding colors. The Strain (μm) relative to the load Moment in Nm. Notably, channels 4 and 5 exhibited similar behavior, reaching a strain limit of 1000 μm, and channel 6 displayed a higher strain limit of approximately 2500 μm. The performance criteria are experimentally verified on the wheel force load cell to compare them with the numerically obtained parameters, either by the simplified methodology or the three-dimensional model analyzed. Thus, the strain conformity matrix is experimentally determined, and the errors associated with mathematical modeling are shown in Table 5, where indexes 1 and 2 represent the simplified and three-dimensional models, respectively. At the same time, subscript 3 represents the parameter obtained experimentally.

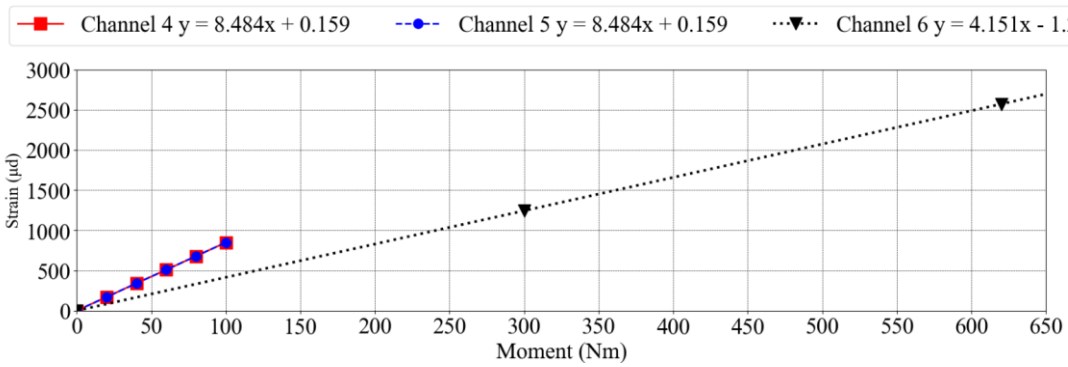

Figure 10. Calibration curves for channels 4, 5 and 6

Notably, in Table 5, the experimental strain conformity matrix has terms in all positions of the matrix; these errors are due to uncertainties in the positioning of the gages in the device, as well as possible failures in the strain-gages adherence and resistivity interference of the electrical circuit wires. Therefore, the errors evaluated only include comparing the terms, which effectively represent the phenomenon of cross-talking in the measurement system. Thus, it is verified that more significant strains were obtained than previously calculated in the numerical analysis for channels 1, 2, and 6, which later represented a greater sensitivity to the system. In contrast, smaller signals are verified in the electrical circuits 4 and 5, lowering load cell sensitivity.

Table 5. Comparison between the load cell compliance matrices [C_t]

$$[\boldsymbol{C_t}]_1 = \begin{bmatrix} 561.24 & 0 & 0 & 13.43 & 0 & 0 \\ 0 & 435.53 & 0 & 0 & 13.43 & 0 \\ -0.57 & 0.44 & 201.90 & 0 & 0 & 0 \\ -33.07 & 0 & 0 & 124.39 & 0 & 0 \\ 0 & 25.69 & 0 & 0 & 124.39 & 0 \\ 0.57 & -0.44 & 43.61 & 0 & 0 & 1089.95 \end{bmatrix} \times \mathbf{10^{-6}} \quad (20)$$

Numeric model

$$[\boldsymbol{C_t}]_2 = \begin{bmatrix} 639.00 & 0 & 0 & 14.50 & 0 & 0 \\ 0 & 494.00 & 0 & 0 & 14.50 & 0 \\ 0 & 0 & 228.00 & 0 & 0 & 0 \\ -36.50 & 0 & 0 & 142.00 & 0 & 0 \\ 0 & 27.50 & 0 & 0 & 142.00 & 0 \\ 0 & 0 & 49.00 & 0 & 0 & 1220.00 \end{bmatrix} \times \mathbf{10^{-6}} \quad (21)$$

Three-dimensional model

$$[\boldsymbol{C_t}]_3 = \begin{bmatrix} 749.00 & -14.80 & -17.20 & 20.70 & 0.90 & 42.00 \\ 11.20 & 571.70 & 0.70 & 1.00 & 22.50 & -22.00 \\ -6.50 & -60.00 & 242.00 & 9.30 & -18.00 & 40.00 \\ -44.20 & 2.20 & 16.00 & 106.00 & -0.10 & 72.00 \\ 77.50 & 32.70 & -16.50 & 8.00 & 107.00 & -48.00 \\ -22.00 & -37.50 & 58.10 & 0.30 & -14.70 & 1540.00 \end{bmatrix} \times \mathbf{10^{-6}} \quad (22)$$

Real model

The errors obtained in the comparison between the simplified and the experimental model is more significant since they consider, besides experimental errors, the numerical inaccuracies caused by the simplifications imposed on the model. However, it is noted that the measured deviations are proportional between the simplified methodology and the three-dimensional model, thus validating the method used in elaborating the force load cell. The force transducer by Nouwens [23], considered $F_X = F_Y = F_Z = 5200$N e $M_X = M_Y = M_Z = 1400$Nm, and the concept incorporated statically indeterminate four-cantilever-spoke and hub force transducers. Nouwens's project proceeded to an optimized geometry using a mathematical model, and strain compliance was calculated using the FE model. Low sensitivities were obtained compared with the present project. Table 6 compares the results obtained by the two conceptions. Considering the design forces and moments, the current concept is better balanced than the Nouwens concept, contributing to an increased sensitivity of the force transducer.

Table 6. Comparisons between Nouwens [23] concept and Delijaicov, et al. concept

Nouwens, concept [23]	Delijaicov, et al. concept
$F_X = F_Y = F_Z = 5200$ N e $M_X = M_Y = M_Z = 1400$Nm	$F_X = 5500$N, $F_Y = 4268$N, $F_Z = 2132$ N, $M_X = 50$ Nm, MY = 50 Nm, $M_Z = 1485$ Nm
$[\boldsymbol{C_t}] = \begin{bmatrix} 341.60 & 0 & 3.10 & 34.00 & 0.90 & 1.60 \\ 0 & 340.90 & 2.50 & -0.70 & 24.50 & 6.70 \\ -13.70 & 13.90 & 306.10 & -0.90 & -1.00 & -12.40 \\ 4.70 & 0 & 0 & 1581.00 & 0 & 0 \\ 0 & -0.10 & 0 & -0.10 & 1583.00 & -11.10 \\ 14.40 & -15.30 & -0.20 & -1.90 & 9.70 & 803.7 \end{bmatrix} x10^{-6}$	$[\boldsymbol{C_t}] = \begin{bmatrix} 749.00 & -14.80 & -17.20 & 20.70 & 0.90 & 42.00 \\ 11.20 & 571.70 & 0.70 & 1.00 & 22.50 & -22.00 \\ -6.50 & -60.00 & 242.00 & 9.30 & -18.00 & 40.00 \\ -44.20 & 2.20 & 16.00 & 106.00 & -0.10 & 72.00 \\ 77.50 & 32.70 & -16.50 & 8.00 & 107.00 & -48.00 \\ -22.00 & -37.50 & 58.10 & 0.30 & -14.70 & 1540.00 \end{bmatrix} x10^{-6}$
1st Modal Frequency (min) = 1153 Hz	1st Modal Frequency (min) = 1351 Hz
Displacement (máx) = not shown	Displacement (máx) = 0.163 mm

Given the geometric symmetry of the two force transducers, cross-talking should be zero, and what was observed can be justified by the non-rigorous positioning of the strain gages and the possible loss of measurements during machining. Several authors [15, 16, 17, 20, 21, 22, 25, 26] have presented concepts of force transducers in wheels with exciting methodologies. However, these works cannot be directly compared to the concept discussed in this paper due to the differences in the geometries and types of efforts used.

4. CONCLUSION

In this work, a decoupled six-axis wheel load cell was successfully designed and optimized using a hybrid parametric optimization approach based on metamodeling techniques. The process was carefully structured, beginning with a fractional factorial design of experiments (DOE) to obtain an initial estimate of the optimization parameters, followed by the use of the finite element method (FEM) to compute the total load cell sensitivity. A gradient-based optimization search was subsequently performed using the Inner Point Optimization Algorithm, with a fallback mechanism that allowed the redefinition of DOE variable ranges if convergence was not achieved. This iterative approach ensured that the optimization continued until convergence was reached.

The methodology employs two different optimization schemes. Once the convergence was attained in the first optimization, a new optimization problem was defined and solved using a different method. This dual-optimization strategy was designed to explore alternative local minima and enhance the robustness of the final solution. When both schemes converge, the more extreme value between the two is selected as the final solution. This scheme ensured the optimal design was robust and could achieve the desired performance characteristics. The DOE simulation results were used as the starting point for the parametric optimization. The final result was a load cell capable of accurately measuring the six force and moment components. The load cell was further validated using a combination of numerical modeling through FEM simulations and experimental calibration. The calibration process, carried out using the MTS 810 universal testing machine, showed a strong correlation between the numerical model and the experimental results, confirming the reliability of the design.

Moreover, mechanical analysis, including von Mises stress distribution, displacement analysis, and vibration mode analysis, was conducted further to evaluate the load cell's structural integrity and performance. The load cell exhibited stress levels around 215 MPa, displacements of approximately 0.16 mm, and a first vibration mode frequency of 1351 Hz, all within acceptable ranges for its intended application. Through this comprehensive design process, simulation, and experimental validation, the developed load cell was shown to meet the criteria for six-axis force and moment measurement. Additionally, the comparison between this design and previous load cell designs in the literature demonstrated good performance in sensitivity and accuracy, particularly in reducing cross-talk effects. This load cell contributes to the field of force measurement, with potential applications in automotive, aerospace, and mechanical engineering testing environments where precise multi-axis load measurements are critical.

ACKNOWLEDGEMENT

The authors would like to thank the University Center of FEI and University Center of Maua Institute of Technology, São Caetano do Sul, São Paulo, Brazil for providing laboratory support and materials to perform the experiments. This work had no funding sources.

AUTHOR CONTRIBUTIONS

Sergio Delijaicov: Conceptualization; Formal analysis; Visualisation; Supervision

Anderson Luiz de Souza Gouvêa: (Methodology; Software; Writing - original draft

Fabrizio Leonardi: Data curation; Formal analysis; Writing - review & editing

Adalto de Farias: Data curation; Writing - review & editing, Visualisation

Éd Cláudio Bordinassi: Formal analysis; Writing - review & editing, validation

CONFLICT OF INTEREST

The authors declare that no financial or non-financial interests are directly linked to the paper submitted for publication.

REFERENCES

[1] J.O. Templeman, B.B. Sheil and T. Sun, "Multi-axis force sensors: A state-of-the-art review," *Sensors and Actuators A: Physical*, vol. 304, p. 111772, 2020.

[2] A.R. Tavakolpour-Saleh, A.R. Setoodeh, and M. Gholamzadeh, "A novel multi-component strain-gauge external balance for wind tunnel tests: Simulation and experiment," *Sensors and Actuators A: Physical*, vol. 247, pp. 172–186, 2016.

[3] R.A.B. Almeida, D.C. Vaz, A.P.V. Urgueira, and A.R.J. Borges, "Using ring strain sensors to measure dynamic forces in wind-tunnel testing," *Sensors and Actuators A: Physical*, vol. 185, pp. 44–52, 2012.

[4] A.R. Tavakolpour-Saleh and M.R. Sadeghzadeh, "Design and development of a three-component force/moment sensor for underwater hydrodynamic tests," *Sensors and Actuators A: Physical*, vol. 216, pp. 84–91, 2014.

[5] A. Blakeborough, D. Clément, M. S. Williams, and N. Woodward, "Novel load cell for measuring axial force, shear force, and bending moment in large-scale structural experiments," *Experimental Mechanics*, vol. 42, no. 1, pp. 115–122, 2002.

[6] E. Korkmaz, B. Bediz, B. A. Gozen, and O.B. Ozdoganlar, "Dynamic characterization of multi-axis dynamometers," *Precision Engineering*, vol. 38, no. 1, pp. 148–161, 2014.

[7] Z. He and T. Liu, "Design of a three-dimensional capacitor-based six-axis force sensor for human-robot interaction," *Sensors and Actuators A: Physical*, vol. 331, p. 112939, 2021.

[8] G.-S. Kim, "Development of a three-axis gripper force sensor and the intelligent gripper using it," *Sensors and Actuators A: Physical*, vol. 137, no. 2, pp. 213–222, 2007.

[9] J.-H. Kim, "Multi-axis force-torque sensors for measuring zero-moment point in humanoid robots: A review," *IEEE Sensors Journal*, vol. 20, no. 3, pp. 1126–1141, 2020.

[10] J. Humm, N. Yoganandan, J. DeRosia, K. Driesslein, J. Avila, and F. Pintar, "A novel posture control device to induce high-rate complex loads for spine biomechanical studies," *Journal of Biomechanics*, vol. 123, p. 110537, 2021.

[11] B. Chen, P. Liu, F. Xiao, Z. Liu, and Y. Wang, "Review of the upright balance assessment based on the force plate," *International Journal of Environmental Research and Public Health*, vol. 18, no. 5, p. 2696, 2021.

[12] A. Song and L. Fu, "Multi-dimensional force sensor for haptic interaction: A review," *Virtual Reality & Intelligent Hardware*, vol. 1, no. 2, pp. 121–135, 2019.

[13] X.C. Akutain, K. Ono, F. Comolli, M. Gobbi, and G. Mastinu, "Further understanding of steering feedback and driver behavior through the application of an instrumented steering wheel," in *Proceeding of 10th International Munich Chassis Symposium 2019*, Wiesbaden, Germany, pp. 481–502, 2019.

[14] M. Gobbi, F. Comolli, F.M. Ballo, and G. Mastinu, "Measurement data obtained by an instrumented steering wheel for driver model development," *Data in Brief*, vol. 30, p. 105485, 2020.

[15] F. Ballo, M. Gobbi, G. Mastinu, and G. Previati, "A six-axis load cell for the analysis of the dynamic impact response of a hybrid III dummy," *Measurement*, vol. 90, pp. 309–317, 2016.

[16] F. Ballo, M. Gobbi, G. Mastinu, and G. Previati, "Advances in force and moments measurements by an innovative six-axis load cell," *Experimental Mechanics*, vol. 54, no. 4, pp. 571–592, 2014.

[17] M. Gobbi, M. Aiolfi, M. Pennati, G. Previati, F. Levi, M. Ribaldone, and G. Mastinu, "Measurement of the forces and moments acting on farm tractor pneumatic tires," *Vehicle System Dynamics*, vol. 43, no. sup1, pp. 412–433, 2005.

[18] T.D. Gillespie, *Fundamentals of Vehicle Dynamics*, Warrendale, PA: SAE International, 1992.

[19] F. Cheli, F. Braghin, M. Brusarosco, F. Mancosu, and E. Sabbioni, "Design and testing of an innovative measurement device for tyre-road contact forces," *Mechanical Systems and Signal Processing*, vol. 25, no. 6, pp. 1956–1972, 2011.

[20] G. Mastinu, M. Gobbi, and G. Previati, "A new six-axis load cell. Part I: Design," *Experimental Mechanics*, vol. 51, no. 3, pp. 373–388, 2011.

21] G. Lin, W. Zhang, F. Yang, H. Pang, and D. Wang, "An initial value calibration method for the wheel force transducer based on memetic optimization framework," *Mathematical Problems in Engineering*, vol. 2013, p. 275060, 2013.

[22] D. Wang, G. Lin, and W. Zhang, "The new method of initial calibration with the wheel force transducer," *Sensor Review*, vol. 34, no. 1, pp. 98–109, 2014.

[23] O.M.M. Nouwens and P. S. Els, "Modeling, fabrication, calibration, and testing of a six-axis wheel force transducer," M.S. thesis, Department of Mechanical and Aeronautical Engeneering, University of Pretoria, Pretoria, South Africa, 2013.

[24] G. Mastinu and M. Gobbi, "Force sensors for active safety, stability enhancement and lightweight construction of road vehicles," *Vehicle System Dynamics*, vol. 61, no. 9, pp. 2165–2233, 2023.

[25] X. Yuan, D. Wang and L. Feng, "A nonlinear decoupling method for wheel force transducer with high-order polynomial model," SAE Technical Paper 2024-01-5085, 2024

[26] L. Feng, S. Wang, J. Shi, A. Song, and P.X. Liu, "An interpretable nonlinear decoupling and calibration approach to wheel force transducers," *IEEE Transactions on Intelligent Transportation Systems*, vol. 25, no. 1, pp. 225–236, 2023.

[27] J.-P. Brüggemann, L. Risse, S. Woodcock, G. Kullmer, and H. A. Richard, "Structural optimization of a wheel force transducer component for more realistic acquisition of vehicle load data and fracture mechanical evaluation," *Applications in Engineering Science*, vol. 5, p. 100032, 2021.

[28] S. Chen, D. Wang, L. Feng, and W. Zhang, "Centralized load decoupling of a rotational multi-axis force sensor for measuring wheel-terrain interaction forces," *Measurement: Journal of the International Measurement Confederation*, vol. 231, p. 114562, 2024.

[29] W. Ren, K. Yu, Y. Zhang, Y. Ge, and Y. Li, "Development and application of a novel high precision six-axis force/torque sensor," *IEEE Access*, vol. 12, pp. 104585-104598, 2024.

[30] A.R. Ahmad, T. Wynn, and C.-Y. Lin, "A comprehensive design of six-axis force/moment sensor," *Sensors*, vol. 21, no. 13, p. 4498, 2021.

[31] S.A. Liu and H.L. Tzo, "A novel six-component force sensor of good measurement isotropy and sensitivities," *Sensors and Actuators A: Physical*, vol. 100, no. 3, pp. 223–230, 2002.

[32] L. Feng, G. Lin, W. Zhang, H. Pang, and T. Wang, "Design and optimization of a self-decoupled six-axis wheel force transducer for a heavy truck," *Proceedings of the Institution of Mechanical Engineers, Part D: Journal of Automobile Engineering*, vol. 229, no. 12, pp. 1585–1610, 2015.

[33] L.-P. Chao and C.-Y. Yin, "The six-component force sensor for measuring the loading of the feet in locomotion," *Materials & Design*, vol. 20, no. 5, pp. 237–244, 1999.

[34] C. Audet and J.E. Dennis Jr., "Analysis of generalized pattern searches," *SIAM Journal on Optimization*, vol. 13, no. 3, pp. 889–903, 2003.